Volume 13
Number 29
7 August 2025
Pages 23149–24162

Journal of Materials Chemistry A

Materials for energy and sustainability

rsc.li/materials-a

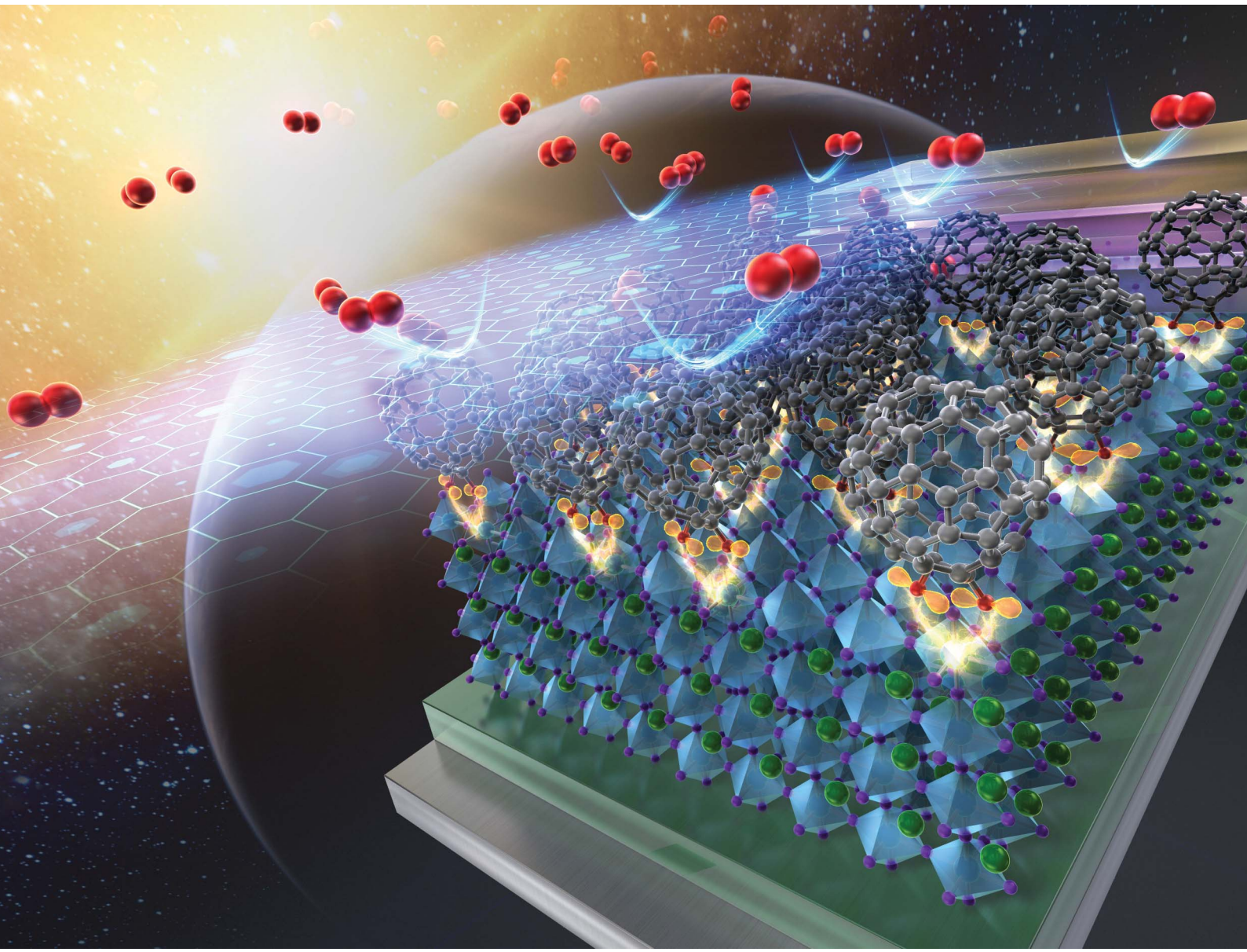

ISSN 2050-7488

ROYAL SOCIETY OF CHEMISTRY

PAPER

Dhruba B. Khadka, Yuko Takeoka, Ryoji Sahara, Yasuhiro Shirai *et al.*

Defect mitigation *via* fullerene-based functional additives for enhanced efficiency and stability in tin perovskite solar cells

Journal of Materials Chemistry A

ROYAL SOCIETY OF CHEMISTRY

PAPER

View Article Online
View Journal | View Issue

Cite this: J. Mater. Chem. A, 2025, 13, 23487

Defect mitigation *via* fullerene-based functional additives for enhanced efficiency and stability in tin perovskite solar cells†

Aman Shukla, ‡[ab] Dhruba B. Khadka, ‡*[a] Chunqing Li, [c] Masahiro Rikukawa, [c] Yuko Takeoka, *[c] Ryoji Sahara, *[d] Masatoshi Yanagida [a] and Yasuhiro Shirai *[a]

Tin-based perovskite solar cells (Sn-PSCs) represent a promising lead-free alternative for photovoltaic applications, however, their oxidation of Sn^{2+} to Sn^{4+}, induces structural defects and compromises device stability and efficiency. In this study, we introduced fullerene-based multifunctional molecules (F-COOH, F-OH, F-OSO_3H) as additives to interact with Sn^{2+} ions, effectively stabilizing tin in its reduced state. These functional additives affect the growth and optoelectronic properties of tin perovskite film. Among these additives, F-COOH significantly suppresses Sn^{4+} formation and non-radiative recombination. Consequently, the device with the F-COOH additive exhibits an increased power conversion efficiency (PCE) from 8.20 to 11.22%, along with improved reproducibility and stability. While additives with –OH and –OSO_3H functional groups also enhance performance, the superior results with F-COOH are attributed to the localized electron density provided by the –COOH group, facilitated by its connection to the fullerene core through a sp^3 hybridized carbon. Device analysis indicated that the F-COOH additive enhances the optoelectronic properties of Sn-PSCs, contributing to a higher diffusion potential while effectively minimizing bulk and interfacial defects. Thus, this work underscores the importance of functional group selection in molecular design to improve the efficiency and stability of Sn-PSCs, paving the way for advanced lead-free solar cell technologies.

Received 3rd December 2024
Accepted 6th May 2025

DOI: 10.1039/d4ta08566c

rsc.li/materials-a

1. Introduction

Lead-based halide perovskite solar cells (Pb-PSCs) have rapidly gained prominence in the field of photovoltaics due to their exceptional power conversion efficiencies (PCEs).[1,2] However, these advantages are tempered by significant challenges, particularly the toxicity of lead.[3] Tin is less toxic than lead, making it a more environmentally benign option. Tin-based halide perovskites (Sn-HP) have similar crystal structures and optoelectronic properties to their lead-based counterparts, offering a theoretical pathway to achieving comparable efficiencies.[4,5] However, the transition to Sn-PSCs introduces new scientific challenges. A major issue is the rapid oxidation of tin from Sn^{2+} to Sn^{4+}, which creates deep trap states in the perovskite lattice, leading to increased non-radiative recombination, lower open-circuit voltage, and reduced overall efficiency. This oxidation also contributes to the intrinsic instability of tin-based perovskites, making them more susceptible to degradation under ambient conditions. Furthermore, the solution processing of Sn-based perovskites is more complex, often resulting in films with inferior crystallinity and higher defect densities compared to lead-based perovskites.[6,7] These defects can significantly impact charge carrier mobility and increase recombination losses, further lowering device performance.

The functional additive technique has emerged as a critical approach to enhancing the performance and stability of Sn-PSCs.[2,8–11] Reducing agents like SnF_2, trivalent doping, hydrazine, or $NaBH_4$ minimize Sn^{4+} defects by stabilizing the Sn^{2+} oxidation state.[12,13] Additives such as alkylammonium halides, polyethylene glycol, and 2-chloroethylphosphonic acid improve film morphology and crystallization, yielding larger grains and fewer defects, which enhance charge transport.[14–16] Solvent additives like DMSO or ethyl acetate control evaporation,

[a]Photovoltaic Materials Group, Center for Green Research on Energy and Environmental Materials, National Institute for Materials Science (NIMS), 1-1 Namiki, Tsukuba, Ibaraki 305-0044, Japan. E-mail: KHADKA.B.Dhruba@nims.go.jp; SHIRAI.Yasuhiro@nims.go.jp

[b]Department of Materials Science & Engineering, National Centre for Flexible Electronics, Indian Institute of Technology Kanpur, Kanpur, Uttar Pradesh 208016, India

[c]Department of Materials and Life Sciences, Sophia University, 7-1, Kioi-cho, Chiyoda-ku, Tokyo 102-8554, Japan. E-mail: y-tabuch@sophia.ac.jp

[d]Computational Structural Materials Group, Research Center for Structural Materials, National Institute for Materials Science (NIMS), 1-2-1, Sengen, Tsukuba, Ibaraki, 305-0047, Japan. E-mail: SAHARA.Ryoji@nims.go.jp

† Electronic supplementary information (ESI) available. See DOI: https://doi.org/10.1039/d4ta08566c

‡ These authors contributed equally to this work.

ensuring uniform films.[17,18] Functional additives also optimize interfacial properties by tuning energy levels, reducing recombination, and enhancing charge extraction.[19–21] For example, self-assembled monolayers with specific dipole moments can be applied to tune the work function of the electron transport layer, optimizing the charge extraction process.[22] Moreover, hydrophobic additives further improve stability by protecting the perovskite layer from moisture-induced degradation.[23]

In recent years, fullerene derivatives have come up as particularly effective additives for this purpose.[24–28] Their ability to interact with the perovskite material at a molecular level makes them especially suited for the passivation of grain boundaries and surface defects in the film. This passivation reduces non-radiative recombination and enhances charge carrier mobility, resulting in higher photocurrent and PCE.[29–31] For instance, Tian *et al.* reported an enhancement in the efficiency of tin-based perovskite solar cells by incorporating a hexyl ester-containing fullerene derivative as a functional additive.[31] This improvement was attributed to the suppression of Sn^{2+} oxidation by the flexible alkyl chains in the additive, which prevent the perovskite layer from interacting with the oxygen. Similarly, Chen and colleagues demonstrated that the quality of the perovskite layer could be enhanced by forming a bulk heterojunction between the –R–NH_2–X group of a fullerene derivative and the perovskite molecules.[32] They also showed that a fullerene derivative with six chlorine atoms could address grain boundary defects by slowing down the crystallization process of the perovskite layer, thereby improving device efficiency. In another study, Liang and colleagues designed a novel fullerene derivative with a porphyrin ring and three pentafluorophenyl groups.[33] This innovative additive efficiently interacts with the perovskite material, facilitating defect passivation and significantly extending the device's lifespan. Choi *et al.* introduced a multifunctional fulleropyrrolidine with triethylene glycol monoethyl ether chains, where the ether component closely interacts with Sn^{2+}, and the fullerene base simultaneously engages with I^-.[34] This dual interaction prevents the formation of Sn^{4+} and I_3^-, resulting in enhanced stability of Sn-based solar cells. Most recently, Chen *et al.* reported a record-breaking efficiency of 15.14% by using pyridyl-substituted fulleropyrrolidones as functional additives in the perovskite precursor solution.[30] This milestone highlights the significant potential of fullerene derivatives in advancing the performance and stability of perovskite solar cells, paving the way for more efficient and durable renewable energy solutions.

Herein, we explored the impact of fullerene derivatives with different functional groups (–COOH, –OH, –OSO_3H) on the efficiency of Sn-PSCs. This study aimed to understand how these functional groups with lone pair-bearing oxygen atoms, attached to the bulky fullerene base, interact with the perovskite matrix to influence key parameters such as film morphology, crystallinity, and the oxidation state of tin. It was found that the derivative with a carboxylic group (–COOH) exhibited the most significant enhancement in device performance from 8.20 to 11.22%. These fullerene-based additives with the carboxylic group were found to be capable of moderating the crystallization process of the perovskite film, resulting in a more uniform morphology with fewer defects. The detailed materials and device analysis corroborate that these functional additives effectively suppressed the oxidation of Sn^{2+} to Sn^{4+} and the recombination states in Sn-PSCs. This work provides valuable insights into the effect of multifunctional functional groups in Sn-PSCs and their crucial role in improving device performance and stability.

2. Results and discussion

2.1. Sn-perovskite film growth with fullerene-based functional additive

Fig. 1a illustrates the fundamental hypothesis of the study. The fullerene-based functional molecules were designed with the expectation that bulky fullerene and those functional groups interact with Sn^{2+} of the $[SnX_6]^{4-}$ octahedra that it may reduce the extent of its oxidation to Sn^{4+}, providing the enhanced structural integrity of Sn-HPs. It is known that functional groups capable of donating electron density or coordinating with tin atoms play a crucial role in stabilizing Sn^{2+}, thereby reducing its tendency to oxidize to Sn^{4+}.[35] Noting that we have used the molecular structures of functional additives shown in Fig. 1b. The additives have functional groups, $\rangle C(COOH)_2$, $(-OH)_2$, and $(-OSO_3H)_2$, which would be hereafter termed as F-COOH, F-OH, and F-OSO_3H, respectively. The synthesis process and characteristics of these fullerene-based additives are given in ESI (Fig. S1–S5 and Tables S1–S3).† From the elemental analysis and TOF-MS data, it is confirmed that all the fullerene compounds are a mixture of adducts (n = 1–5). We fabricated the Sn-HP ($FA_{0.80}MA_{0.05}PEA_{0.15}SnI_3$) films with fullerene-based functional molecules as additives.

To understand the effect of additives on crystal growth, X-ray diffraction (XRD) patterns of Sn-HP films (Fig. 1c) were measured. The most prominent XRD peaks obtained correspond to (100) and (200) crystallographic planes, which are consistent with the orthorhombic phase, aligning with previously reported data.[36] A slightly narrower FWHM of the dominant XRD pattern suggests improvement in crystallinity with Sn-HP film with additives (Fig. S6†). Furthermore, the characteristic XRD peaks of the perovskite layer with different additives do not shift from that of the control layer, suggesting no incorporation of fullerene-functional additives into the lattice of the host crystal.

Similarly, the absorption and PL spectra of Sn-HP with additive films were measured to evaluate the effect of additives on photophysical properties. Fig. 1d exhibits a nuanced impact on characteristic absorption spectra with slight variations in absorbance. Among the different additives, the film with the F-COOH additive demonstrates a slightly higher absorption response, indicating a better optoelectronic response. The characteristic absorption edge, as depicted in the inset, shows a band edge of ~892 nm. PL spectra of these films are depicted in Fig. 1e. There is no shifting in characteristics PL peak ~892 nm, which is equivalent to ~1.395 ± 0.02 eV corresponding to the band edge, indicates non-interference of these additives into the electronic picture of pristine perovskite structure. Importantly, a variation in PL spectra intensity

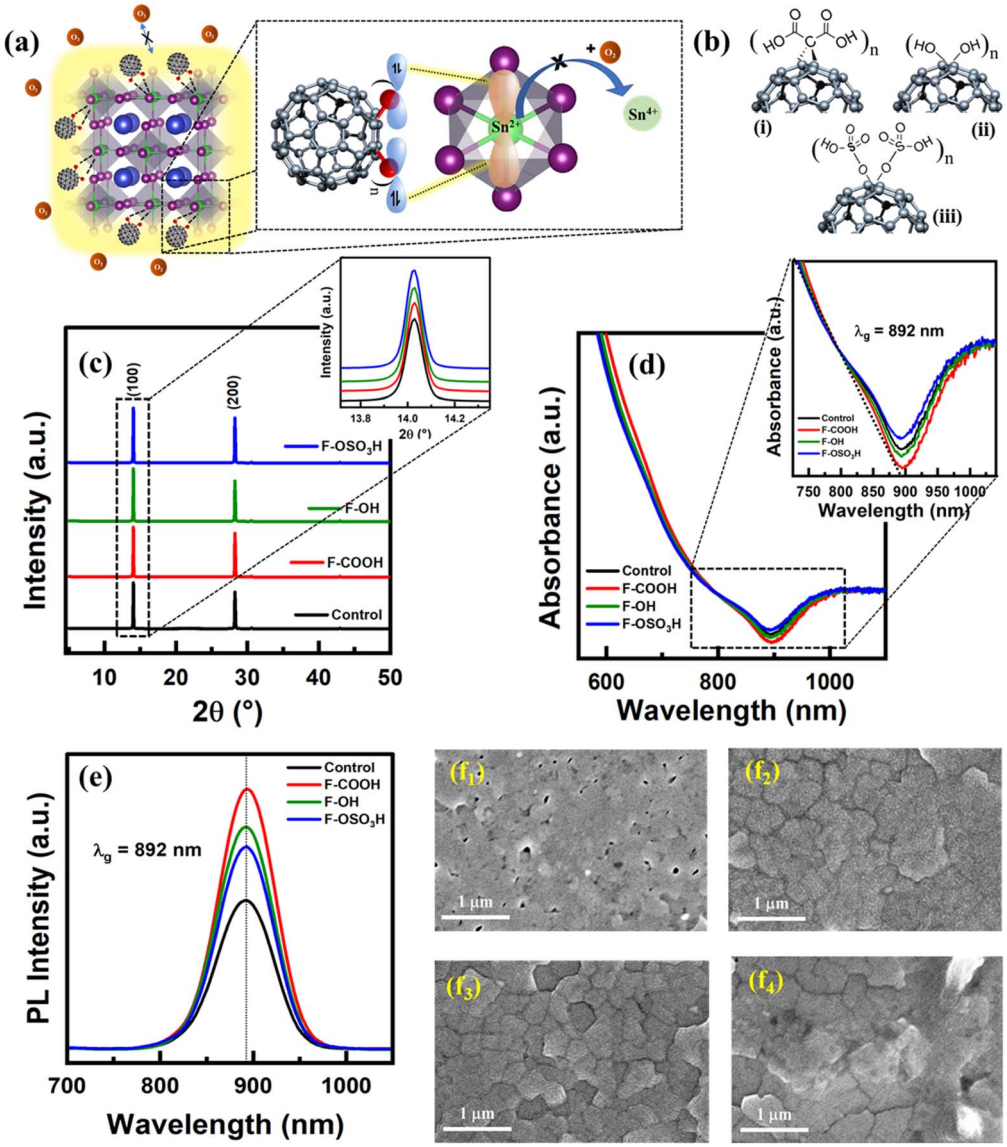

Fig. 1 (a) Schematic interaction of fullerene-based additive with Sn-HP. (b) Molecular structure of different additives employed in the study ((i) $C_{60}(\triangleright C(COOH)_2)_n$ (F-COOH), (ii) $C_{60}((OH)_2)_n$ (F-OH), (iii) $C_{60}((OSO_3H)_2)_n$ (F-OSO_3H). (c) XRD patterns (with a zoomed view), (d) absorbance spectrum (with a zoomed view), (e) PL spectrum, and (f) SEM images of perovskite film without and with functional additives ((f_1) control, (f_2) F-COOH, (f_3) F-OH, (f_4) F-OSO_3H).

indicates the effect of additives in a passivating defect in the Sn-HP film. An intensified PL spectrum for Sn-HP with F-COOH additive corroborates improved film quality and reduced non-radiative recombination.[37] Further, PL spectra of Sn-HP films with varying concentrations of F-COOH additive (Fig. S7†) suggest that an excessive additive concentration induces a nonradiative recombination state within the perovskite films.[38,39] With higher additive concentrations, additional defect states or traps in the perovskite film promote non-radiative recombination, where the energy from excited carriers is lost as heat rather than emitted as light, thus diminishing the PL intensity.

Fig. $1f_1$–f_4 display the SEM images of the Sn-HP films, providing insights into how different functional additives influence the film morphology, particularly in terms of surface coverage and defect density. The SEM image of the control film (Fig. $1f_1$) shows pinholes with poor film coverage, which are detrimental to the overall performance of the perovskite layer.[40] While the SEM images (Fig. $1f_2$–f_4) of Sn-HP with F-COOH, F-OH, and F-OSO_3H additives demonstrate significant improvements in surface coverage and film uniformity. These additives play a crucial role in enhancing the quality of the perovskite film by reducing the number of pinholes and defects. The presence of fewer defects and more complete surface coverage leads to better charge transport, ultimately improving the optoelectronic properties of the films. Among the additives, F-COOH shows comparatively better film morphology, yielding a film with the most uniform coverage that could be due to the strong

interactions between the functional carboxyl (–COOH) groups of the F-COOH additive and the tin perovskite polyhedral. These interactions play a key role in regulating the crystallization process during film formation, promoting more controlled and uniform growth of perovskite crystals. However, the amount of additives also plays a critical role in determining the film quality. SEM images of films with higher concentrations of F-COOH reveal irregularities (Fig. S8†). This suggests that beyond the optimal concentration, the additive begins to interfere with the perovskite crystallization process, possibly by introducing excess nucleation sites or disrupting the film's uniform growth. Consequently, the film becomes more prone to imperfections, undermining the benefits initially provided by the additive.

2.2. Effect of fullerene-based functional additive on Sn-PSC device performance

To investigate the effect of fullerene-based functional molecules on photovoltaic performance, a complete device has been fabricated with the inverted configuration of ITO/PEDOT/Sn-HP/ICBA/BCP/Ag. The cross-sectional SEM images of Sn-PSCs are shown in Fig. 2a and b, where enhanced crystalline growth is evident in the device with F-COOH additive compared to the control device. The effect of various functional additives on the device parameters is summarized in Tables 1 and S4.† The current density–voltage (J–V) characteristics are detailed in Fig. 2c. The control device exhibited a PCE of 8.20% with open-circuit voltage (V_{OC}) ~ 0.769 V, a short-circuit current density (J_{SC}) ~ 17.44 mA cm^{-2}, and a fill factor (FF) ~ 61.29%. The Sn-PSCs with F-COOH achieved a significant increase in PCE to 11.22%, with improvements across all parameters (V_{OC} to 0.841 V, a J_{SC} to 19.31 mA cm^2, and FF to 69.12%). Moreover, the addition of the F-COOH additive significantly reduced the hysteresis observed in the forward and reverse scans of the J–V curves (Fig. S9†). The notable enhancement in performance reflects the ability of the –COOH group to interact with the perovskite material, leading to better film morphology and crystallinity. We also evaluated devices incorporating the F-COOH additive at varying concentrations. The J–V characteristics are shown in Fig. S10,† and the corresponding device parameters are summarized in Table S5.† The higher concentration of F-COOH may lead to an increase in irregularities in the perovskite film morphology. Excessive additives can disrupt the uniformity of the film as given in Fig. S8,† creating more defects or uneven crystallization, which are deleterious to device performance as shown in Table S5.†

Furthermore, Sn-PSCs with additives containing hydroxyl (–OH) and sulfonic ester (–OSO_3H) groups also exhibited an

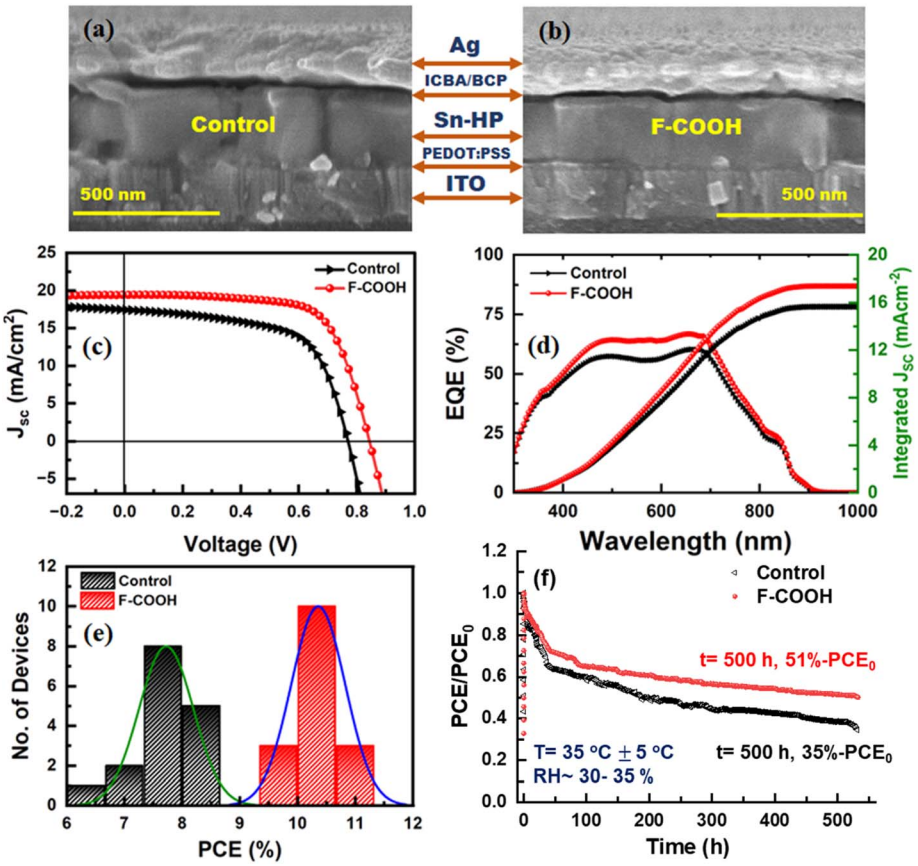

Fig. 2 Cross-sectional SEM images of devices (a) control and (b) with F-COOH additive. (c) J–V curves of devices. (d) EQE spectra. (e) Statistical histogram of corresponding device efficiencies (16 devices from 4 batches). (f) Operational stability of Sn-PSCs under MPPT conditions and air ambient (ISOS-L-1).

Table 1 Device parameters of Sn-PSCs with and without additives. The average values and standard deviation (SD) are obtained from 4 batches (16 devices)

Device	Scan direction	J_{SC} (mA cm^{-2})	V_{OC} (V)	FF (%)	PCE (%)	Average (PCE ± SD)
Control	F	16.47	0.783	59.66	7.69	7.76 ± 0.52
	R	17.44	0.769	61.29	8.20	
F-COOH	F	19.27	0.838	65.51	10.57	10.32 ± 0.51
	R	19.31	0.841	69.12	11.22	
F-OH	F	18.48	0.819	64.59	9.77	9.38 ± 0.46
	R	18.67	0.825	66.22	10.19	
F-OSO_3H	F	17.85	0.801	65.51	9.36	8.97 ± 0.47
	R	18.36	0.813	65.42	9.76	

increase in PCE, reaching 10.19% and 9.76%, respectively. These results indicate that both –OH groups and –OSO_3H also contribute to improving the optoelectronic properties of the perovskite film, likely through enhanced molecular interaction and better crystallization processes.[41,42] These improvements suggest that the additive effectively stabilizes the interface between the perovskite and the charge transport layers and mitigates ion migration and trap-assisted recombination.[38,43] We will discuss this in detail in succeeding sections.

Fig. 2d shows the external quantum efficiency (EQE) of the control device and the best Sn-PSC with F-COOH additive. The EQE spectrum for Sn-PSC with F-COOH additive reveals a noticeable enhancement across the entire spectral range, indicating the suppression of recombination activities in bulk and at the interfaces of the device.[44] The J_{SC} values (15.67 mA cm^{-2} for control and 17.50 mA cm^{-2} for the device with F-COOH) obtained from integrating the EQE spectrum are in the close range of those obtained from *J–V* curves. Additionally, the band edge of the EQE spectra (Fig. S11†) is estimated to be ~1.428 and 1.425 ± 0.02 eV for control and with F-COOH additive. These values are in close agreement with the band edge estimation from absorption and PL spectra.

Moreover, the statistical data (Fig. 1e), provided in Table S4† and graphically illustrated in Fig. S12,† offer a detailed comparison of batches of Sn-PSCs with additives. The control device demonstrates an average PCE of 7.76%, while those values for devices with additives are higher. Importantly, the statistical data reveal that the distribution of device parameters across batches has narrowed for devices with additives compared to the control device, suggesting higher reproducibility of device parameters and, hence device performance. Enhanced reproducibility is critical for ensuring that solar cells perform consistently, which is a key requirement for large-scale manufacturing and commercialization.

To study the effect on device stability, we collected the operational stability of unencapsulated control and device with F-COOH additive under maximum power point tracking (MPPT) conditions and air ambient, adopting stability assessment ISOS-L-1.[45] The normalized efficiencies of respective Sn-PSCs are presented in Fig. 2f. The control device experiences a significant drop in efficiency to 35% of its initial value after 500 hours. This rapid decline in performance suggests that the control device is highly susceptible to degradation, likely due to factors such as moisture, oxygen ingress, or intrinsic instability within the perovskite layer.[46] In contrast, the device incorporating the F-COOH additive exhibits markedly improved stability, retaining more than 51% of its initial efficiency even after 500 hours. This enhanced stability highlights the beneficial effect of the F-COOH additive in mitigating the degradation mechanisms commonly observed in perovskite solar cells.[46,47] It is likely attributed to the additive's ability to interact with the perovskite structure during film formation, leading to better crystallization, reduced defect density, and stronger resistance to environmental factors. The water contact angles of the Sn-HP film with fullerene derivatives (Fig. S15†) show a higher water contact angle compared to the control film, suggesting a higher hydrophobicity film. The increase in hydrophobicity with fullerene additive also supports the superior device stability of Sn-PSC with F-COOH additive. This improvement implies that the F-COOH additive appears to play a protective role by passivating surface defects, stabilizing grain boundaries, and inducing water resistivity, which are often points of vulnerability in perovskite films where degradation initiates. It reduces degradation over time and contributes to a more stable and durable solar cell. However, further research is warranted to explore additional methods to enhance stability even more.

2.3. Effect of fullerene-based functional additives on surface chemistry

To study the effect of additives on surface chemistry, we investigated the Sn-HP films using X-ray photoelectron spectroscopy (XPS). The XPS spectra (Fig. 3a and b) show characteristic peaks of Sn 3d core at 485.2 and 493.5 eV for Sn^{2+}, and at 486.2 and 494.3 eV for Sn^{4+}.[37,48] The analysis of deconvoluted peaks reveals that the control film has a higher ionic percentage (19.6%) of Sn^{4+}, compared to the film with the F-COOH additive (11.2%). It suggests that the F-COOH additive effectively mitigates the oxidation of Sn^{2+}, thereby reducing the extent of Sn^{2+} oxidation and enhancing the overall quality of the perovskite film. Also, the XPS spectra of the I 3d level (Fig. 3c and d) for the film containing the F-COOH additive exhibit a noticeable shift toward higher binding energy compared to that of the control film. The binding energy shift implies that the additive may be contributing to a more stable ionic lattice by influencing the local electronic structure, particularly around the tin and iodine atoms. Similarly, as for other functional additives, the deconvoluted XPS peaks of the Sn 3d also demonstrated a significant

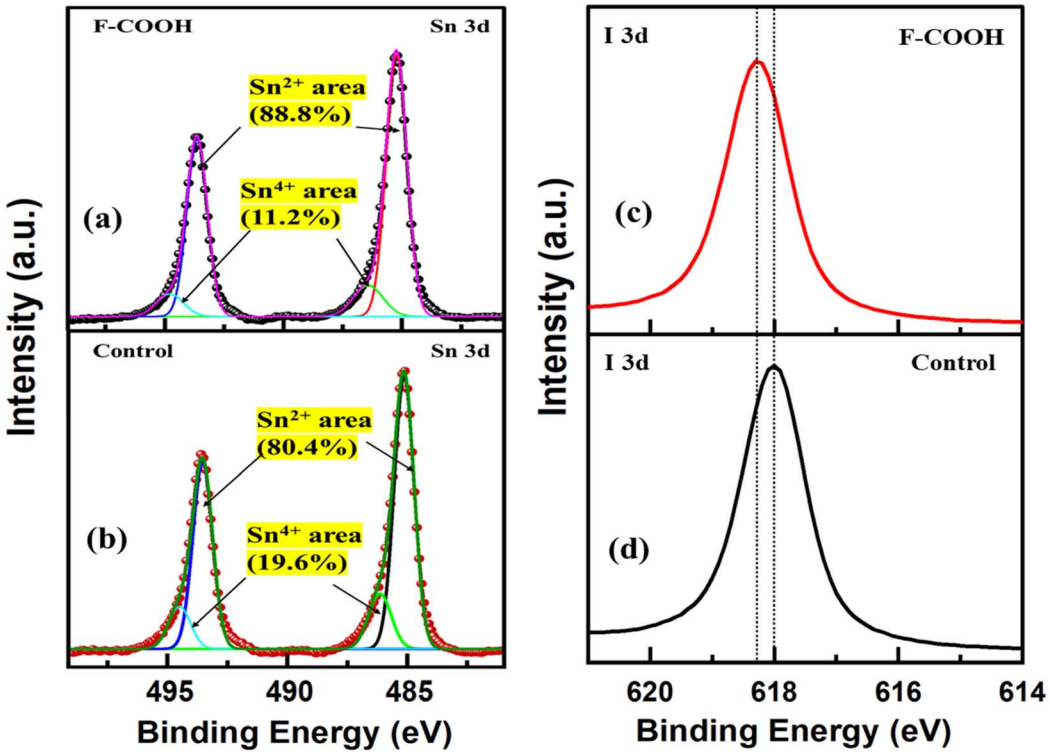

Fig. 3 XPS spectra: (a and b) Sn 3d, (c and d) I 3d of the surface of the Sn-HP films without and with F-COOH additive.

reduction in the ionic percentage of Sn^{4+} species compared to the control film (Fig. S13†). Specifically, the Sn^{4+} content decreases from 19.6% to 12.1% and 13.7% for Sn-HP films containing F-OH and F-OSO_3H, respectively. XPS results support the hypothesis that the functional groups attached to fullerene interact with Sn^{2+} centers in the perovskite film, effectively shielding them from oxidation. These functional groups are strategically positioned within a molecular framework of high electron density, forming a protective barrier around Sn^{2+}. While pristine fullerene is highly electron-withdrawing, the incorporation of –COOH, –OH, and –OSO_3H alters the electron distribution, creating localized electron-rich regions near the functional sites. This enhanced electron density strengthens the coordination between these groups and Sn^{2+}, stabilizing it and suppressing oxidation. By reducing interactions with oxidizing species, this effect significantly improves the stability and performance of Sn-PSCs with fullerene-based functional additives.

In fundamental chemical aspects, the ability of these additives to mitigate Sn^{2+} oxidation can be attributed to their inherent nature and interactions with the Sn^{2+} ion.[37] Functional groups capable of donating electron density or coordinating with tin atoms play a crucial role in stabilizing Sn^{2+}. Particularly, the carboxylate group in F-COOH can bind to tin *via* coordination, offering a protective barrier that helps to maintain a higher proportion of Sn^{2+}. Importantly, the –COOH group in F-COOH is not directly attached to the fullerene ring but instead is connected through a sp^3-hybridized carbon atom ($C_{60}(>C(COOH)_2)_n$). This structural feature localizes the electron density on the carboxylate group, making it more available for interaction with Sn^{2+}, contributing to the improved stability and quality of the resulting perovskite film. On the other hand, the hydroxyl group (–OH) in F-OH also contributes electron density to the fullerene ring through hydrogen bonding, which can help stabilize Sn^{2+}. Although the electron-donating power of the hydroxyl group is generally stronger than that of the carboxylate group, in this specific molecular framework, the –OH group is directly attached to an sp^2-hybridized carbon of the fullerene ring, which is more acidic than sp^3 hybridized carbon.[49] This configuration results in higher acidity of the carbon and partial delocalization of the electron density over the fullerene ring, reducing the availability of electron density for Sn^{2+} stabilization as compared to F-COOH. The sulfate ester group (–OSO_3H) in F-OSO_3H also provides some stabilization of Sn^{2+} through conjugation, but the electron-withdrawing nature of the –SO_3H group limits the electron donation to the tin ion. As a result, F-OSO_3H is less effective in stabilizing Sn^{2+} compared to F-COOH or F-OH. The hierarchy of electron-donating ability and defect passivation effectiveness among the derivatives follows the trend: F-COOH > F-OH > F-OSO_3H, in agreement with prior experimental observations and device performance trends. This observation is in line with a report on the effect of the interaction of $HCOO^-$ anions and Sn^{2+} cations by Wang and co-workers.[50] To validate this hypothesis further, these fullerene derivatives were investigated through DFT-calculated electrostatic surface potential (ESP) analysis. The ESP mapping (Fig. S16a–d†) reveals that F-COOH exhibits significant negative potential around the –COOH group, facilitating effective

coordination with undercoordinated Sn^{2+} sites. In contrast, the ESP maps of F-OH & F-OSO_3H display relatively less negative potentials, reflecting weaker passivation capability compared to F-COOH. Hence, the superior performance of F-COOH arises from its optimal molecular structure that facilitates efficient electron donation and robust Sn^{2+} stabilization, as confirmed by ESP analysis. These findings validate the proposed molecular interaction mechanism and underscore the critical importance of sp^3-hybridized anchoring points and carefully modulated electrostatic environments in engineering highly efficient and stable tin-based perovskite solar cells.

2.4. Effect on transient photo characteristics and defect calculations

To explore the effect on carrier recombination, we measured the time-resolved photoluminescence (TRPL) characteristics (Fig. 4a and S14†) and calculated carrier lifetimes for the Sn-HP film with different additives, summarized in Table S6.† The Sn-HP with additives exhibits the longest carrier lifetime. Specifically, the Sn-HP film with the F-COOH additive is 3.31 ns, which is significantly longer compared to the control film (1.70 ns), suggesting a lower defect density in the Sn-HP with the F-COOH additive. In the same line, the Sn-HP with F-OH and F-OSO_3H also showed an enhanced lifetime of 3.09 ns and 2.84 ns. The improved lifetime is likely due to the controlled growth of the film's morphology, resulting in larger grain sizes, enhanced crystallinity, and reduced defect density. These improvements reduce non-radiative recombination and enhance the film quality. The trend observed in the TRPL data for the various films is consistent with the *J–V* performance results, further confirming that the F-COOH additive has the most positive impact on the perovskite film's optoelectronic properties.

Moreover, to gain insights into the photocarrier dynamics, we conducted transient photo characteristics, transient photovoltage (TPV), and transient photocurrent (TPC) measurements. The TPV curve (Fig. 4b) for the F-COOH device exhibits a notably slower decay compared to the control device, indicating a significantly longer carrier lifetime of 15.44 μs from 10.62 μs. This extended carrier lifetime is typically a sign of fewer trap states within the device, which would otherwise act as recombination centers for carriers.[51,52] It corroborates that Sn-PSC with F-COOH additive reduces trap-assisted recombination and contributes to enhanced performance, supporting the conclusion that this functional additive is key to achieving better device stability and efficiency. Similarly, the TPC curve (Fig. 4c) assesses the effect on the interface quality of the device. Sn-PSC with F-COOH additive shows a faster current decay time of 5.56 μs, compared to the control (6.38 μs). This faster decay is indicative of more efficient charge carrier extraction in the Sn-PSC with F-COOH, one of the critical factors for improving solar cell performance. These results further support the benign effect of F-COOH additives on material quality and device properties. Furthermore, the capacitance measurements were conducted to gain critical insights into the device's charge carrier dynamics, interface states, trap states, and defect density profile.[53,54] Fig. 5a shows the capacitance–frequency (*C–f*) spectra of devices. The control device exhibits a noticeably higher capacitance compared to the F-COOH-modified device, which is attributed to higher charge accumulation and ionic motion in the control device. This suggests that the additive might be suppressing ionic movement or mitigating its effects on charge accumulation.[55] The device with the F-COOH additive demonstrates a lower capacitance over the frequency range, indicating that the additive has likely reduced the density of trap states.[43,46]

To evaluate the effects on the defect profile, we analyzed the capacitance spectra with Mott–Schottky (M–S) plots and carrier profile as given by $N_{CV} = -\frac{2}{q\varepsilon_0\varepsilon_s}\left[\frac{d}{dV}\left(\frac{1}{C(V)^2}\right)\right]^{-1}$, where N_{CV} represents carrier density calculated from the capacitance–voltage (*C–V*) curve, *C* is the capacitance per unit area, ε_0 is the permittivity of free space, ε_s is the dielectric constant of the perovskite material. The MS plot, as shown in Fig. 5b, compares the control device with the device containing the F-COOH additive. The device with the F-COOH additive reveals a higher diffusion potential (V_D) of 0.824 V compared to the control (0.702 V). This increment in V_D aligns well with the enhancement in V_{OC} in Sn-PSC. This result suggests that the F-COOH additive strengthens the separation of electron–hole pairs, reduces recombination losses, and ultimately contributes to higher V_{OC}.[51]

Fig. 5c depicts the spatial distribution of charge carriers across the device calculated from the *C–V* measurements. This analysis provides insights into how charge carriers are distributed within the bulk of the active layer and at the interface regions, where recombination and charge transport play

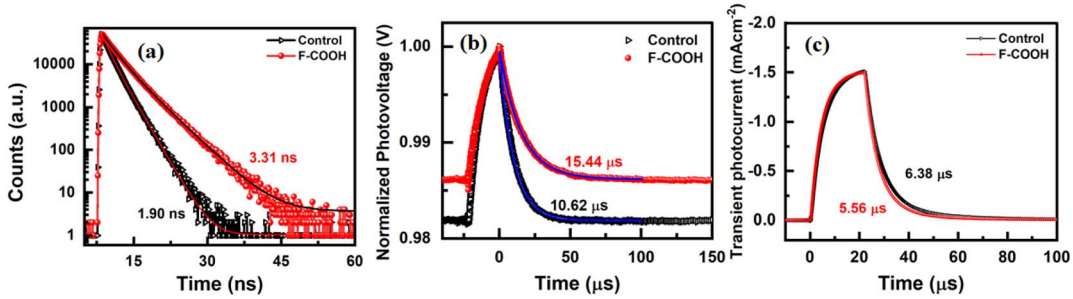

Fig. 4 (a) TRPL decay spectra of Sn-HP films (control and with F-COOH additive). (b) TPV decay curves, and (c) TPC decay curves of devices (control and with F-COOH additive).

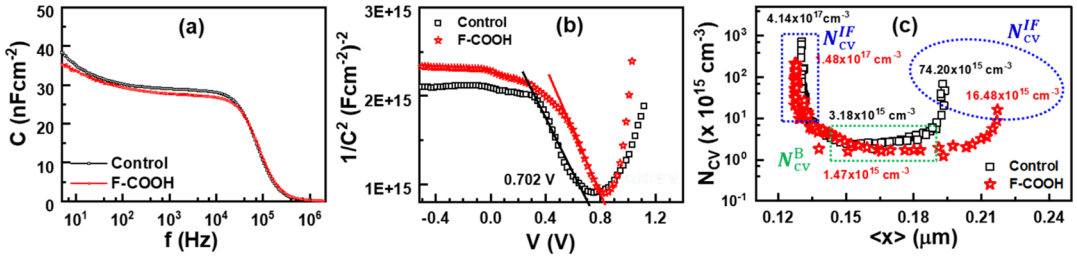

Fig. 5 Capacitance characteristics of devices: (a) *C*–*f* spectra under darkness, (b) Mott–Schottky plots, (c) carrier profile of the device without and with F-COOH additive.

a crucial role in device performance. It has been documented that the N_{CV} profile accounts for the carrier distribution (free carrier and defect density)[47,56,57] and ion or charge accumulation at the interface[53] in thin-film solar cells. In the control device, the bulk carrier density (N_{CV}^{B}) is estimated to be 3.18×10^{15} cm^{-3}. While the device with the F-COOH additive showed a reduced bulk carrier density of 1.47×10^{15} cm^{-3}. This reduction suggests that the F-COOH additive is effective in mitigating defects within the bulk perovskite layer that can capture and recombine charge carriers. This trend of reduced carrier profile extends to the interface region as well. The control device exhibits an interfacial carrier density (N_{CV}^{IF}) of 7.42×10^{16} cm^{-3}, while the F-COOH-modified device shows a significantly lower density of 1.65×10^{16} cm^{-3}. This reduction at the interface implies that the F-COOH additive is also effective at passivating interfacial defects, which are often hotspots for charge recombination due to discontinuities in the crystal structure and imperfect layer alignment. The decrease in the *C*–*V* carrier profile correlates with improved carrier lifetimes resulting from defect passivation.

Theoretical insights were obtained by performing DFT calculations considering a slab model with a SnI_2-terminated

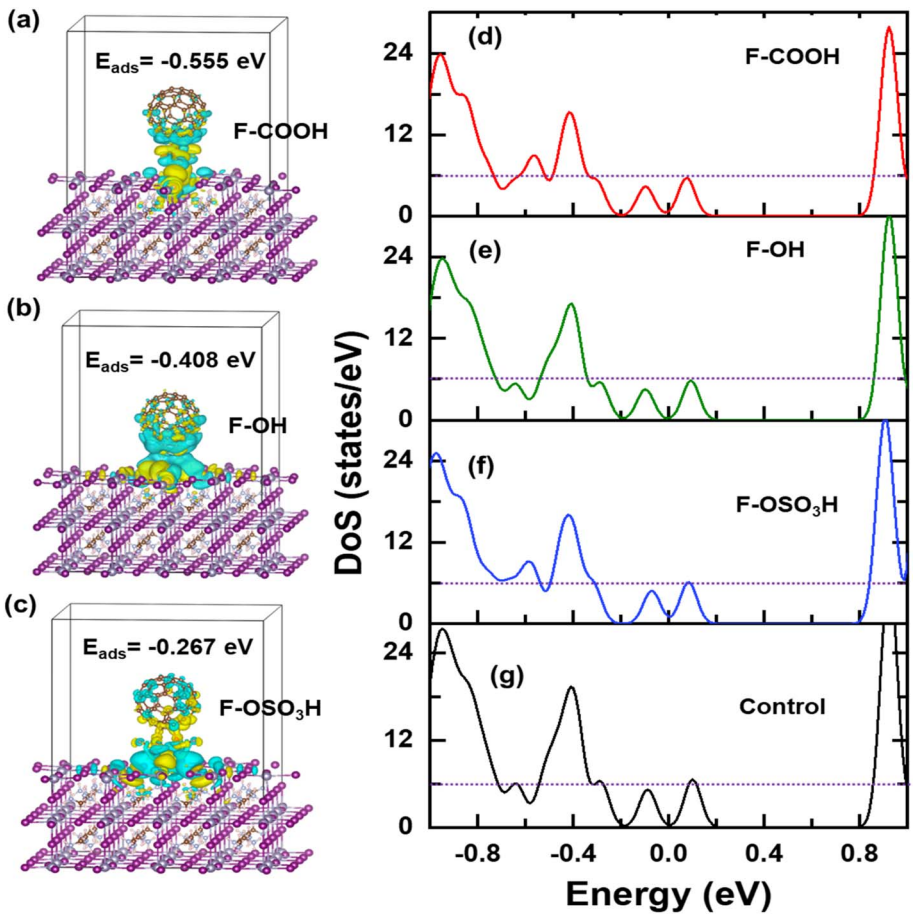

Fig. 6 Theoretical calculations on the effect of fullerene derivatives on Sn-perovskite. Charge density difference and adsorption energy for (a) F-COOH/Sn-perovskite, (b) F-OH/Sn-perovskite, (c) F-OSO_3H/Sn-perovskite. Density of states of (d) F-COOH, (e) F-OH, (f) F-OSO_3H, and (g) control-based Sn-perovskite from DFT calculations.

perovskite surface as described in our earlier report[58] to investigate the interaction between fullerene derivatives and the tin-based perovskite. The charge density difference of fullerene functional derivatives on the defective Sn-perovskite surface (Fig. 6a–c) indicates mitigation of the density of defect states.[37] The adsorption energies (Fig. 6a–c and S16d–f†) reveal a clear trend: F-COOH exhibits the strongest binding with the Sn-perovskite surface (−0.555 eV), followed by F-OH (−0.408 eV) and F-OSO_3H (−0.267 eV). The stronger adsorption energy of F-COOH suggests a more robust chemical interaction with undercoordinated Sn^{2+} sites, leading to more effective defect passivation compared to F-OH and F-OSO_3H. This inference is further supported by the density of states (DOS) calculation as depicted in Fig. 6d–g, which shows a reduction in defect states near the Fermi level up to some extent upon fullerene functionalization, particularly in the case of F-COOH. The stronger binding and superior defect mitigation effect of F-COOH correlate well with experimental observations, including reduced trap-assisted recombination from capacitance measurements, longer carrier lifetimes from TRPL analysis, and improved photovoltage stability from TPV measurements.[59]

Thus, theoretical and experimental results reveal that the fullerene-based functional additives induce a strong adsorption on the Sn-perovskite surface. This interaction plays a crucial role in mitigating the oxidation of Sn^{2+} to Sn^{4+} and enhancing the perovskite layer's material chemistry integrity. The fullerene derivatives demonstrate a notable improvement in both efficiency and stability of the devices. A comprehensive device analysis combined with theoretical insights substantiates the experimentally observed performance enhancements, highlighting the potential of fullerene derivatives as effective functional additives for advancing Sn-based perovskite photovoltaics.

3. Conclusion

This study explored the impact of fullerene derivatives with various functional groups (–COOH, –OH, –OSO_3H) on the efficiency of tin-based perovskite solar cells, with a particular focus on how these functional groups interact with the perovskite matrix. The findings demonstrate that the fullerene derivative with a carboxylic group (–COOH) significantly enhances device performance, increasing the power conversion efficiency from 8.20% to 11.22% and extending the stability of devices significantly. This improvement is attributed to the additive's ability to moderate the crystallization process of the perovskite film, leading to a more uniform morphology with fewer defects and effectively suppressing the oxidation of Sn^{2+} to Sn^{4+}. These results not only highlight the potential of fullerene-based additives in improving the stability and efficiency of tin-based perovskite solar cells but also offer a promising pathway for the development of more reliable and high-performance renewable energy solutions. Future research should focus on optimizing these additives and exploring additional functional groups to further enhance the performance of next-generation perovskite solar cells.

4. Experimental section

4.1. Materials and precursor solution

As mentioned, all chemicals were purchased from commercial suppliers and used as received. Formamidinium iodide (FAI, 99.9%, luminescent), methylammonium iodide (Sigma-Aldrich), SnI_2 (Sigma-Aldrich), and SnF_2 (Sigma-Aldrich), poly(3,4-ethylenedioxythiophene):poly(styrene sulfonate) (PEDOT:PSS) (Clevious, A14083), ICBA (one material, 99% purity) and BCP (Sigma-Aldrich, 99% purity) were purchased and used as received. For the fabrication of Sn-HP films, the precursors were prepared by dissolving FAI (0.8 M), MAI (0.05 M), PEAI (0.15), SnI_2 (1 M), and SnF_2 (0.1 M) for perovskite solution in 3 ml of dimethyl sulfoxide (DMSO) solvent overnight at room temperature. Similarly, precursors with fullerene-based multifunctional functional molecules (F-COOH, F-OH, and F-OSO_3H) were prepared by adding additives. ICBA (one material, 99% purity) solution (3 wt%) dissolved in anhydrous chlorobenzene (CB) was used for coating the electron transport layer (ETL). A saturated BCP solution was prepared by dissolving 3 mg in 3 ml of anhydrous isopropanol. All the solutions were filtered using 0.45 mm syringe filters just before the deposition to avoid the risk of unwanted particles in the precursor solution.

4.2. Synthesis of fullerene compounds

Fullerene (99.95% MTR Ltd) derivatives (F-COOH, F-OH, and F-OSO_3H) were synthesized at Sophia University. A detailed synthesis method and related characterizations are given in the ESI.†

4.3. Device fabrication

Solar cell devices were fabricated on pre-cleaned patterned indium tin oxide (ITO) coated glass substrates (15 Ω sq^{-1}). The ITO substrates were pre-cleaned in an ultrasonic bath with detergent, pure water, and 2-propanol, followed by an ultraviolet-ozone treatment for 15 minutes to remove the organic residuals. A thin HTM layer (30 nm) of PEDOT:PSS was deposited onto the ITO substrate by spin coating at 4000 rpm and subsequently dried at 150 °C for 20 min on a hot plate in ambient air. Then, the substrates were transferred into a nitrogen-filled glove box (<1.0 ppm O_2 and H_2O), and the rest of the steps were carried out inside the glove box. The Sn-HP precursor was spin-coated at 6000 rpm for 90 s (ramping slope 3 s) followed by dripping 150 ml of CB at the 60^{th} second. Then, to promote the crystallization, those as-grown Sn-HP films were simply placed on a hot plate at 60 °C for 1 min and 85 °C for 15 min. A passivation layer of 4-fluoro-benzohydrazide (4F-BHZ) (Fig. S17†) was dynamically deposited at 5000 rpm for 50 s, followed by annealing at 75 °C for 5 min.[58] For the ETM layer, ICBA was spin-coated on top at 1500 rpm for 30 s and 4000 rpm – 5 s and then annealed at 75 °C – 5 min, followed by dynamic deposition of a thin BCP layer spinning at 5000 rpm for 30 s, which was annealed at 70 °C – 5 min. To complete the device structure, the samples were then transferred into the evaporation chamber connected to the glove box for metal contact deposition. Finally, 140 nm of Ag was thermally

evaporated at a pressure < 10^{-4} Pa. Four device sections with an area of ~0.26 cm^2 are confined in a 2.5 cm × 3 cm ITO substrate.

4.4. Device characterization

The morphology of the films was studied, and cross-sectional images were taken using a high-resolution scanning electron microscope (SEM) at a 5 kV accelerating voltage (Hitachi, S-4800). X-ray diffraction (XRD) patterns of fabricated Sn-HP films were collected using an advanced X-ray diffractometer (Rigaku SmartLab, CuK_α radiation, λ = 1.54050 Å). The absorption spectra of the various films were measured using a UV-vis-NIR spectrometer (UV-2600i, Shimadzu). The photoluminescence (PL) spectra were collected using a micro-PL spectrometer (HORIBA, LabRamHR-PL NF(UV-NIR)) ~532 nm laser diode (10 mW cm^{-2}) as an excitation source. The carrier lifetimes were measured with a fluorescence lifetime spectrometer (Quantaurus-τ from Hamamatsu-Photonics K.K., C11367) equipped with ~405 nm laser diode (typical peak power of 400 mW) at 200 kHz repetition rate. XPS spectra were obtained using a Versa Probe II (ULVAC-PHI, Japan). The current density–voltage (*J–V*) curves were measured at the scan rate of 0.05 V s^{-1} under 1 sun with an AM1.5G spectral filter (100 mW cm^{-2}) coupled with an MPPT system (SystemHouse Sunrise Corp.). The light intensity was calibrated by a silicon (Si) diode (BS-520BK). For the stability test, the encapsulated devices were measured under MPPT conditions and air ambient. The external quantum efficiency (EQE) spectra were obtained using a spectrometer (SM-250IQE, Bunkoukeiki, Japan). The transient photovoltage and photocurrent data were measured using a commercial PAIOS system (PAIOS V.4.3). A pulse intensity was used to induce a spike in photovoltage. The capacitance spectra (*C–f*) were taken from PAIOS v. 4.3 software, which scans from 20 Hz to 2 MHz at 50 mV AC in the dark at a bias voltage of 0 V. The *C–V* measurements were taken at 20 kHz with a voltage amplitude of 30 mV AC in the dark.

4.5. Density functional theory calculation

First-principles calculations based on density functional theory (DFT) were performed by adopting a slab model of a SnI_2-terminated surface[38] using the Vienna *ab initio* simulation package[60] which implements the projector-augmented wave method.[61] The influence of vdW interactions between the molecules and the Sn-HP film was considered.

For the exchange–correlation function, the Perdew–Burke–Ernzerhof function,[38] was used. A $2\sqrt{2} \times 2\sqrt{2} \times 1$ slab supercell of (001) surface, containing 5 layers, was built from a bulk tetragonal phase of $FASnI_3$ (space group: *P*4/*mbm*), with a vacuum region of about 22 Å was added in the *z* direction. The kinetic energy cutoff of 400 eV and the convergence criterion of 10^{-4} eV for the self-consistent loop were employed. To explore stable adsorption sites of the molecule, a SnI_2-terminated surface with Sn-vacancy (V_{Sn}) defect was used, on which a molecule was placed, based on the insight from the previous work.[62] Gamma point sampling was employed for the Brillouin zone integration. The adsorption energy of the molecule was evaluated as $E_{ads} = E_{system\ with\ molecule} - E_{system\ without\ molecule} - \mu_{mol}$ where $E_{system\ with\ molecule}$ and $E_{system\ without\ molecule}$ are energies of the surfaces with and without a molecule additive, respectively, and μ_{mol} is the chemical potential of the molecule. The total energy computed for an isolated gas phase was used for μ_{mol}.

Data availability

The data supporting this article have been included as part of the ESI.†

Conflicts of interest

The authors declare no competing financial interest.

Acknowledgements

This work was supported by The Hitachi Global Foundation, Kurata grants (#1572), and partially by the JST-ALCA-Next Program (Grant Number JPMJAN23B2), Japan. We extend our sincere gratitude to Dr Kentaro Kikuchi for his valuable assistance in synthesizing fullerene derivative compounds. We also acknowledge the technical support provided by Yamaguchi Kazuo-San (XPS) and Takahashi Hiromi (XRD) from the NIMS Battery Research Platform for their respective measurement and analysis contributions. The calculations in this study were performed using the Numerical Materials Simulator at the National Institute for Materials Science (NIMS). Aman Sukla expresses appreciation to the National Institute for Materials Science (NIMS) for the opportunity to participate in the short-term "NIMS Internship Program." The authors are deeply thankful to Prof. Monica Katiyar and Prof. Kenjiro Miyano for their insightful comments and constructive suggestions in this work.

References

1 M. A. Green, E. D. Dunlop, M. Yoshita, N. Kopidakis, K. Bothe, G. Siefer, X. Hao and J. Y. Jiang, *Prog. Photovolt.: Res. Appl.*, 2025, **33**, 3–15.
2 D. B. Khadka, Y. Shirai, M. Yanagida, J. W. Ryan, Z. Song, B. G. Barker, T. P. Dhakal and K. Miyano, *Sol. RRL*, 2023, **7**, 2300535.
3 G. Schileo and G. Grancini, *J. Mater. Chem. C*, 2021, **9**, 67–76.
4 M. A. Kamarudin, D. Hirotani, Z. Wang, K. Hamada, K. Nishimura, Q. Shen, T. Toyoda, S. Iikubo, T. Minemoto, K. Yoshino and S. Hayase, *J. Phys. Chem. Lett.*, 2019, **10**, 5277–5283.
5 F. Hao, C. C. Stoumpos, P. Guo, N. Zhou, T. J. Marks, R. P. H. Chang and M. G. Kanatzidis, *J. Am. Chem. Soc.*, 2015, **137**, 11445–11452.
6 M. Aldamasy, Z. Iqbal, G. Li, J. Pascual, F. Alharthi, A. Abate and M. Li, *Phys. Chem. Chem. Phys.*, 2021, **23**, 23413–23427.
7 J. Cao and F. Yan, *Energy Environ. Sci.*, 2021, **14**, 1286–1325.
8 B. Li, H. Di, B. Chang, R. Yin, L. Fu, Y. N. Zhang and L. Yin, *Adv. Funct. Mater.*, 2021, **31**, 1–9.

9 S. J. Lee, S. S. Shin, Y. C. Kim, D. Kim, T. K. Ahn, J. H. Noh, J. Seo and S. Il Seok, *J. Am. Chem. Soc.*, 2016, **138**, 3974–3977.
10 T. J. Macdonald, L. Lanzetta, X. Liang, D. Ding and S. A. Haque, *Adv. Mater.*, 2023, **35**, 2206684.
11 C. Sun, H. Zhang, S. Cheng, J. Chen, Y. Xing, Z. Nan, P. Yang, Y. Wang, X. Zhao, L. Xie, C. Tian and Z. Wei, *Adv. Mater.*, 2024, **36**, 2410248.
12 J. Sanchez-Diaz, R. S. Sánchez, S. Masi, M. Krecmarová, A. O. Alvarez, E. M. Barea, J. Rodriguez-Romero, V. S. Chirvony, J. F. Sánchez-Royo, J. P. Martinez-Pastor and I. Mora-Seró, *Joule*, 2022, **6**, 861–883.
13 T. Wang, H. Loi, Q. Cao, G. Feng, Z. Guan, Q. Wei, C. Chen, M. Li, Y. Zhu, C. Lee and F. Yan, *Adv. Mater.*, 2024, **36**, 2402947.
14 J. Wang, M. A. Uddin, B. Chen, X. Ying, Z. Ni, Y. Zhou, M. Li, M. Wang, Z. Yu and J. Huang, *Adv. Energy Mater.*, 2023, **13**, 1–8.
15 Z. Liu, P. Liu, T. He, L. Zhao, X. Zhang, J. Yang, J. Yang, H. Yang, H. Liu, H. Liu, R. Qin, R. Qin and M. Yuan, *ACS Appl. Mater. Interfaces*, 2020, **12**, 26670–26679.
16 K. Cao, H. Ning, N. Xu, W. Zuo, Y. Zhang, M. Yang, J. Xia, L. Liu and S. Chen, *J. Mater. Chem. A*, 2024, **12**, 17444–17452.
17 M. K. A. Mohammed, S. Singh, A. K. Al-Mousoi, R. Pandey, J. Madan, D. Dastan and G. Ravi, *RSC Adv.*, 2022, **12**, 32611–32618.
18 X. Jiang, H. Li, Q. Zhou, Q. Wei, M. Wei, L. Jiang, Z. Wang, Z. Peng, F. Wang, Z. Zang, K. Xu, Y. Hou, S. Teale, W. Zhou, R. Si, X. Gao, E. H. Sargent and Z. Ning, *J. Am. Chem. Soc.*, 2021, **143**, 10970–10976.
19 D. B. Khadka, Y. Shirai, M. Yanagida and K. Miyano, *ACS Appl. Energy Mater.*, 2021, **4**, 12819–12826.
20 X. Zhou, W. Peng, Z. Liu, Y. Zhang, L. Zhang, M. Zhang, C. Liu, L. Yan, X. Wang and B. Xu, *Energy Environ. Sci.*, 2024, **17**, 2837–2844.
21 Z. Zhao, M. Sun, F. Xiang, X. Wu, Z. Fink, Z. Huang, J. Gao, H. Ding, P. Tan, C. Yuan, Y. Yang, N. A. Emelianov, L. A. Frolova, Z. Xiao, P. A. Troshin, T. P. Russell, J. Zhu, Y. Li and Q. Hu, *J. Mater. Chem. A*, 2025, **13**, 409–417.
22 J. Roe, J. G. Son, S. Park, J. Seo, T. Song, J. Kim, S. O. Oh, Y. Jo, Y. Lee, Y. S. Shin, H. Jang, D. Lee, D. Yuk, J. G. Seol, Y. S. Kim, S. Cho, D. S. Kim and J. Y. Kim, *ACS Nano*, 2024, **18**, 24306–24316.
23 G. Wang, J. Bi, M. Lei, J. Chang and F. Meng, *Energy Fuels*, 2022, **36**, 7755–7762.
24 K. Liu, S. Chen, J. Wu, H. Zhang, M. Qin, X. Lu, Y. Tu, Q. Meng and X. Zhan, *Energy Environ. Sci.*, 2018, **11**, 3463–3471.
25 M. Lee, D. Kim, Y. K. Lee, H. Koo, K. T. Lee and I. Chung, *ACS Appl. Energy Mater.*, 2020, **3**, 5581–5588.
26 Z. Li, X. Li, M. Wang, M. Cai, X. Shi, Y. Mo, X. Chen, D. Ren, M. Yang, X. Liu, R. Jia, N. V. Medhekar and S. Dai, *ACS Appl. Energy Mater.*, 2022, **5**, 108–115.
27 E. Hou, J. Chen, J. Luo, Y. Fan, C. Sun, Y. Ding, P. Xu, H. Zhang, S. Cheng, X. Zhao, L. Xie, J. Yan, C. Tian and Z. Wei, *Angew. Chem., Int. Ed.*, 2024, **136**, e202402775.
28 J. Chen, J. Luo, Y. Li, X. Chen, Z. Song, E. Hou, C. Sun, H. Zhang, S. Cheng, Y. Xing, S. Chen, X. Zhao, L. Xie, C. Tian and Z. Wei, *Angew. Chem., Int. Ed.*, 2025, **137**, e202420150.
29 W. Yu, X. Sun, M. Xiao, T. Hou, X. Liu, B. Zheng, H. Yu, M. Zhang, Y. Huang and X. Hao, *Nano Res.*, 2022, **15**, 85–103.
30 J. Chen, J. Luo, E. Hou, P. Song, Y. Li, C. Sun, W. Feng, S. Cheng, H. Zhang, L. Xie, C. Tian and Z. Wei, *Nat. Photonics*, 2024, **18**, 464–470.
31 C. Tian, K. Lin, J. Lu, W. Feng, P. Song, L. Xie and Z. Wei, *Small Methods*, 2020, **4**, 1900476.
32 J. Chen, C. Tian, C. Sun, P. Yang, W. Feng, L. Zheng, L. Yang, E. Hou, J. Luo, L. Xie and Z. Wei, *Energy Environ. Mater.*, 2024, **7**, 1–8.
33 Y. Liang, P. Song, H. Tian, C. Tian, W. Tian, Z. Nan, Y. Cai, P. Yang, C. Sun, J. Chen, L. Xie, Q. Zhang and Z. Wei, *Adv. Funct. Mater.*, 2022, **32**, 1–8.
34 J. Choi, S. J. Yang, S. G. Han, W. Sung, D. Yoo and K. Cho, *Chem. Mater.*, 2023, **35**, 1148–1158.
35 P. J. Smith, *Chemistry of Tin*, Springer Netherlands, Dordrecht, 1998.
36 K. Nishimura, M. A. Kamarudin, D. Hirotani, K. Hamada, Q. Shen, S. Iikubo, T. Minemoto, K. Yoshino and S. Hayase, *Nano Energy*, 2020, **74**, 104858.
37 J. Chen, J. Luo, E. Hou, P. Song, Y. Li, C. Sun, W. Feng, S. Cheng, H. Zhang, L. Xie, C. Tian and Z. Wei, *Nat. Photonics*, 2024, **18**, 464–470.
38 D. B. Khadka, Y. Shirai, M. Yanagida, T. Tadano and K. Miyano, *Chem. Mater.*, 2023, **35**, 4250–4258.
39 Y. Su, J. Yang, G. Liu, W. Sheng, J. Zhang, Y. Zhong, L. Tan and Y. Chen, *Adv. Funct. Mater.*, 2022, **32**, 2109631.
40 W. Liao, D. Zhao, Y. Yu, C. R. Grice, C. Wang, A. J. Cimaroli, P. Schulz, W. Meng, K. Zhu, R.-G. Xiong and Y. Yan, *Adv. Mater.*, 2016, **28**, 9333–9340.
41 H. Kim, Y. H. Lee, T. Lyu, J. H. Yoo, T. Park and J. H. Oh, *J. Mater. Chem. A*, 2018, **6**, 18173–18182.
42 C.-H. Kuan, J.-M. Chih, Y.-C. Chen, B.-H. Liu, C.-H. Wang, C.-H. Hou, J.-J. Shyue and E. W.-G. Diau, *ACS Energy Lett.*, 2022, **7**, 4436–4442.
43 M. A. Kamarudin, D. Hirotani, Z. Wang, K. Hamada, K. Nishimura, Q. Shen, T. Toyoda, S. Iikubo, T. Minemoto, K. Yoshino and S. Hayase, *J. Phys. Chem. Lett.*, 2019, **10**, 5277–5283.
44 A. Nakane, H. Tampo, M. Tamakoshi, S. Fujimoto, K. M. Kim, S. Kim, H. Shibata, S. Niki and H. Fujiwara, *J. Appl. Phys.*, 2016, **120**, 064505.
45 M. V. Khenkin, *et al.*, *Nat. Energy*, 2020, **5**, 35–49.
46 C. C. Boyd, R. Cheacharoen, T. Leijtens and M. D. McGehee, *Chem. Rev.*, 2019, **119**, 3418–3451.
47 D. B. Khadka, Y. Shirai, M. Yanagida and K. Miyano, *ACS Appl. Energy Mater.*, 2021, **4**, 11121–11132.
48 D. B. Khadka, Y. Shirai, M. Yanagida and K. Miyano, *J. Mater. Chem. C*, 2020, **8**, 2307–2313.
49 C. Qiu, L. Jiang, Y. Gao and L. Sheng, *Mater. Des.*, 2023, **230**, 111952.
50 H. Yu, Z. Zhang, H. Dong, X. Li, Z. Liu, J. Huang, Y. Fu, Y. Shen and M. Wang, *ACS Energy Lett.*, 2024, **9**, 5870–5878.
51 G. Yang, Z. Ren, K. Liu, M. Qin, W. Deng, H. Zhang, H. Wang, J. Liang, F. Ye, Q. Liang, H. Yin, Y. Chen, Y. Zhuang, S. Li,

B. Gao, J. Wang, T. Shi, X. Wang, X. Lu, H. Wu, J. Hou, D. Lei, S. K. So, Y. Yang, G. Fang and G. Li, *Nat. Photonics*, 2021, **15**, 681–689.

52 D. B. Khadka, Y. Shirai, M. Yanagida, H. Ota, A. Lyalin, T. Taketsugu and K. Miyano, *Nat. Commun.*, 2024, **15**, 882.

53 K. Miyano, M. Yanagida and Y. Shirai, *Adv. Energy Mater.*, 2020, **10**, 1903097.

54 D. B. Khadka, Y. Shirai, M. Yanagida, T. Masuda and K. Miyano, *Sustainable Energy Fuels*, 2017, **1**, 755–766.

55 K. Miyano, M. Yanagida, N. Tripathi and Y. Shirai, *J. Phys. Chem. Lett.*, 2016, **7**, 2240–2245.

56 D. B. Khadka, Y. Shirai, M. Yanagida and K. Miyano, *ACS Appl. Mater. Interfaces*, 2019, **11**, 7055–7065.

57 C. W. Warren, E. T. Roe, D. W. Miller, W. N. Shafarman and M. C. Lonergan, *Appl. Phys. Lett.*, 2017, **110**, 203901.

58 D. B. Khadka, Y. Shirai, R. Sahara, M. Yanagida and K. Miyano, *Small*, 2024, 2410048.

59 D. B. Khadka, Y.-C. Kuo, Y. Z. Li, M. Waqas, Y.-J. Xu, M. Yanagida, H. Nishihara, K. Tsukagoshi, M. M. C. Chou, Y. Shirai and Y.-C. Wang, *ACS Appl. Mater. Interfaces*, 2025, **17**(18), 26813–26822.

60 G. Kresse and J. Furthmüller, *Phys. Rev. B:Condens. Matter Mater. Phys.*, 1996, **54**, 11169–11186.

61 G. Kresse and D. Joubert, *Phys. Rev. B:Condens. Matter Mater. Phys.*, 1999, **59**, 1758–1775.

62 J. P. Perdew, A. Ruzsinszky, G. I. Csonka, O. A. Vydrov, G. E. Scuseria, L. A. Constantin, X. Zhou and K. Burke, *Phys. Rev. Lett.*, 2008, **100**, 136406.

